processes

MDPI

Communication

Co-Precipitated $Mn_{0.15}Ce_{0.85}O_{2-\delta}$ Catalysts for NO Oxidation: Manganese Precursors and Mn-Ce Interactions

Yuxi Gao [1,2,†], Baofang Jin [1,3,†], Xiaodong Wu [1,*], Zhenguo Li [4], Rui Ran [1] and Duan Weng [1]

1 Key Laboratory of Advanced Materials of Ministry of Education of China, School of Materials Science and Engineering, Tsinghua University, Beijing 100084, China
2 BOE Technology Group Co., Ltd., Beijing 100176, China
3 State Key Laboratory of Multiphase Complex Systems, Institute of Process Engineering, Chinese Academy of Sciences, Beijing 100190, China
4 National Engineering Laboratory for Mobile Source Emission Control Technology, China Automotive Technology & Research Center, Tianjin 300300, China
* Correspondence: wuxiaodong@tsinghua.edu.cn
† These two authors contributed equally to this work.

Abstract: Two $Mn_{0.15}Ce_{0.85}O_{2-\delta}$ mixed oxides were synthesized by a co-precipitation method using $Mn(NO_3)_2$ and $KMnO_4$ as the manganese precursors, respectively. Structural analyses by X-ray powder diffraction and Raman spectroscopy reveal the formation of MnO_x-CeO_2 solid solutions. The $Mn_{0.15}Ce_{0.85}O_{2-\delta}$ catalyst prepared from the high-valent manganese precursor exhibits higher activity for the catalytic oxidation of NO. The advantage of $KMnO_4$ is related to the improved redox property of the catalyst as supported by H_2 temperature-programmed reduction (TPR) and O_2 temperature-programmed desorption (TPD). The Mn-Ce interactions create more Mn^{4+}, Ce^{3+} and oxygen vacancies on the $KMnO_4$-synthesized mixed oxides based on the Raman and X-ray photoelectron spectra (XPS).

Keywords: solid solutions; precursor; oxidation state; lattice defects; NO oxidation

Citation: Gao, Y.; Jin, B.; Wu, X.; Li, Z.; Ran, R.; Weng, D. Co-Precipitated $Mn_{0.15}Ce_{0.85}O_{2-\delta}$ Catalysts for NO Oxidation: Manganese Precursors and Mn-Ce Interactions. *Processes* **2022**, *10*, 2562. https://doi.org/10.3390/pr10122562

Academic Editor: Maria Jose Martin de Vidales

Received: 8 November 2022
Accepted: 1 December 2022
Published: 1 December 2022

1. Introduction

NO oxidation is an important reaction for environmental protection, such as NO oxidative adsorption [1], fast selective catalytic reduction (SCR) of NO [2,3], lean NO_x adsorption (LNT) [4], and NO_2-assisted soot oxidation [5,6]. Pt catalysts are widely considered as the most efficient catalysts despite their high costs. Ceria is one of the cheap catalytic materials and plays important roles in many catalytic reactions owing to easy redox cycle between Ce^{4+} and Ce^{3+}.

The redox property of ceria can be improved by interaction with transition metals, e.g., Fe^{x+} [7], Mn^{x+} [8], Co^{x+} [9], and Cu^{x+} [10]. Among the mixed oxides, MnO_x-CeO_2 catalysts are the most favorable ones due to a favorable synergistic effect between these two metal oxides. Nevertheless, their catalytic activities for NO oxidation have not been fully explored. Machida et al. [11] found that the enhanced NO oxidative adsorption of the mixed oxides is facilitated by both the high NO oxidation activity of MnO_x and the strong NO_x adsorption ability of CeO_2. They pointed out that the active sites for NO oxidation were Mn species accompanied with reversible sorption/desorption of lattice oxygens based on XPS and O_2-TPD studies [12]. Li et al. [13] evidenced the existence of a synergistic mechanism between the oxides in the MnO_x-CeO_2. They found that Mn-Ce-O_x improved the activities of NO oxidation due to the increased surface area and the enhanced dispersion of MnO_x with the addition of Ce. In our previous study [14], this synergistic mechanism was further verified in a tight-contact mixture of MnO and CeO_2 via a so-called long-ranged electronic interaction, which created more Mn^{4+} and oxygen vacancies compared with the loose-contact mixture of the oxides.

It is acceptable that such an electronic interaction would be much more significant in the solid solutions of MnO_x and CeO_2 synthesized by chemical methods. In this work, two $Mn_{0.15}Ce_{0.85}O_{2-\delta}$ mixed oxides were synthesized by co-precipitation using different manganese precursors. Detailed microstructural and surface property characterizations were carried out to establish structure-performance relationships of the catalysts for NO oxidation.

2. Experimental

2.1. Catalyst Preparation

Two $Mn_{0.15}Ce_{0.85}O_{2-\delta}$ (corresponding to a Mn/Ce molar ratio of 15/85) were synthesized by a co-precipitation method with different manganese precursors. KOH solution was added dropwise to a precursor solution of $Mn(NO_3)_2$ (aqueous solution, 50 wt.%, Aladdin, China) and $Ce(NO_3)_3{\cdot}6H_2O$ (99.99 wt.%, Aladdin) to adjust the pH to 10.5 and stirred at 50 °C for 2 h. In order to ensure the complete removal of potassium ions, the precipitate was filtrated and washed at least four times. After drying the solid at 110 °C for 12 h and calcination at 500 °C for 6 h in air, the obtained catalyst was denoted as MnCe-L (the low-valent manganese sample). Another $Mn_{0.15}Ce_{0.85}O_{2-\delta}$ catalyst was prepared by the same method except using $KMnO_4$ (Aladdin) as the manganese precursor, and the obtained catalyst was denoted as MnCe-H (the high-valent manganese sample). Due to electronic interactions between Mn^{x+} and Ce^{x+} and thermal oxidation/reduction of metal ions during calcination, different manganese and cerium ions co-existed in the final products.

For reference, Mn_3O_4 and CeO_2 were synthesized by a similar precipitation method using $Mn(NO_3)_2$ and $Ce(NO_3)_3{\cdot}6H_2O$ as the precursors, respectively. The physical mixture of Mn_3O_4 and CeO_2 at a Mn/Ce molar ratio of 15/85 was prepared by mixing Mn_3O_4 and CeO_2 powders using a spatula for two minutes. MnO_2 (Aladdin) and MnO (Aladdin) were also used for reference.

2.2. Activity Measurement

Temperature-programmed oxidation (TPO) of NO was performed in a fixed-bed reactor connected to an infrared spectrometer Nicolet iS10 (Thermo Fisher, Waltham, MA, USA) with a gas mixture of 1000 ppm NO/10% O_2/N_2 (500 mL·min^{-1}) as the reaction gas. In order to smooth airflow and heat dissipation, the catalyst powders (100 mg) were mixed with silica pellets (300 mg) using a spoon. Then, the mixture was placed in a tubular quartz reactor, and was heated to 700 °C at a rate of 10 °C·min^{-1}.

2.3. Catalyst Characterization

X-ray diffraction (XRD) patterns were measured on a D8 ADVANCE diffractometer (Bruker, Germany) using Cu K_α radiation (λ = 0.15418 nm). The XRD patterns ranged between 10° and 80° at 0.02° intervals and recorded at a scanning speed of 4°·min^{-1}.

Specific surface areas of the samples were determined on an automatic surface analyzer (F-Sorb 3400, Gold APP Instrument, Beijing, China) by the four-point Brunauer–Emmett–Teller (BET) method. Prior to the experiment, the samples were degassed at 200 °C for 2 h to remove the molecules adsorbed on the sample surface.

X-ray fluorescence analysis (XRF) was performed on a Shimadzu instrument (1800 Kyoto, Japan) to determine the elemental contents of the samples.

Raman spectra were collected on a confocal micro-Raman apparatus (Aurora J300, IDSpec, Hong Kong, China) using an Ar^+ laser with a wavelength of 632.8 nm.

X-ray photoelectron spectra (XPS) were performed on a PHI-Quantera SXM system equipped with Al K_α radiation. The data was corrected based on C 1*s* (284.8 eV).

Temperature-programmed reduction (TPR) of H_2 was conducted on an Auto Chem II Chemisorption Analyzer (Micromeritics, USA). A 50 mg sample was pretreated with a

He flow (50 mL·min^{-1}) at 450 °C for 30 min. After being cooled down to room temperature, the sample was heated in 10% H_2/Ar (50 mL·min^{-1}) to 900 °C with a rate of 10 °C·min^{-1}.

Temperature-programmed desorption (TPD) of O_2 was carried out on the Auto Chem II Chemisorption Analyzer. After purging in He at 300 °C for 1 h, 200 mg sample was exposed to 10% O_2/He at 50 °C for 1 h. The reactor was heated to 900 °C at a rate of 10 °C·min^{-1} after flushed by He for half an hour.

3. Results and Discussion

3.1. NO Oxidation Activity

Figure 1 shows the NO oxidation activities of the mixed oxide catalysts and reference samples. The dotted NO_2 profile was drawn by the thermodynamic equilibrium of NO + O_2 ↔ NO_2. Pure CeO_2 shows low NO conversions (<30%) within the whole temperature range, which is ascribed to its relatively poor redox behavior. The NO oxidation activity of manganese oxides increases with the valance of the metal ions, i.e., MnO_2 > Mn_3O_4 > MnO. Specifically, Mn_3O_4 exhibits a quite strong ability to oxidize NO to NO_2 and reaches the maximum NO conversion (59%) at 337 °C. The mixture of Mn_3O_4 and CeO_2 shows NO conversions between the two monoxide components. Given the same composition of the mixed oxides, both the co-precipitated samples present much higher catalytic performance than the mechanical mixture. MnCe-H even shows slightly higher activity than Mn_3O_4, while MnCe-L has somewhat lower NO conversions at the temperatures lower than 360 °C. Considering the dominating species of Ce in the mixed oxides, these facts demonstrate strong synergistic effects between manganese oxide and ceria in the co-precipitated samples, which depend importantly on the preparation methods and the precursor adopted. Although MnO_2 exhibits higher NO oxidation activity than $Mn_{0.15}Ce_{0.85}O_{2-\delta}$ mixed oxides, the poor thermal stability [15], poor sulfur resistance [16] and relatively high cost limit its industrial applications. It is well known that phase transformation of MnO_2 to Mn_2O_3 occurs readily at 200–720 °C [17], while $Mn_{0.15}Ce_{0.85}O_{2-\delta}$ catalysts maintain high NO oxidation activity after calcination at 650 °C [18].

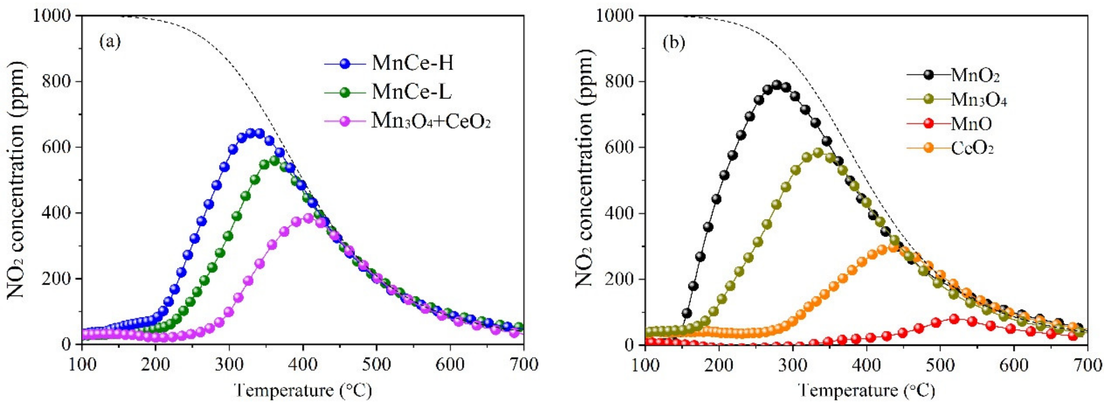

Figure 1. NO_2 evolution during NO-TPO tests over (**a**) $Mn_{0.15}Ce_{0.85}O_{2-\delta}$ mixed oxides and (**b**) reference oxide catalysts. Reaction conditions: NO = 1000 ppm, O_2 = 10%, N_2 in balance, GHSV = 30,000 h^{-1}.

3.2. Structural Properties

The powder XRD patterns of the samples are shown in Figure 2a. The diffraction peaks of the precipitated manganese oxide and ceria correlate well with the characteristics of tetragonal Mn_3O_4 and cubic CeO_2, respectively [19]. Only diffraction peaks of ceria are observed in the patterns of two $Mn_{0.15}Ce_{0.85}O_{2-\delta}$ mixed oxides. The absence of any MnO_x-related peaks implies highly dispersed state of MnO_x clusters in the matrix of ceria or the formation of MnO_x-CeO_2 solid solutions [20]. Table 1 lists the lattice constants and mean crystallite sizes of the samples calculated according to Cohen's method and Williamson-Hall equation, respectively. Apparently, the calculated lattice constants of ceria in the mixed oxides are smaller than that of pure ceria. The shrinkage of the ceria crystal cell is attributed to the incorporation of smaller manganese ions (Mn^{4+}: 0.053 nm; Mn^{3+}: 0.065 nm; Mn^{2+}: 0.083 nm) into the ceria (Ce^{3+}: 0.114 nm; Ce^{4+}: 0.097 nm) lattice to form metastable pseudo-solid solutions [11,21]. It herein indicates the substitution of cerium by manganese in the crystal cell of ceria in the co-precipitated mixed oxides. Furthermore, MnCe-L presents a larger lattice parameter than MnCe-H, which is associated with the incorporation of a larger amount of large Mn^{2+} cations in the former mixed oxides. As listed in Table 1, Mn_3O_4 presents an exceptionally lower BET surface area owing to significant grain growth of manganese oxide [12]. It is also noted that MnCe-H shows a higher specific surface area than MnCe-L due to the smaller crystallites. No potassium was detected by XRF, and thus its influence can be excluded. The atomic ratio of Mn/(Mn + Ce) is close to 0.15 for both the mixed oxides, correlating with the theoretical value.

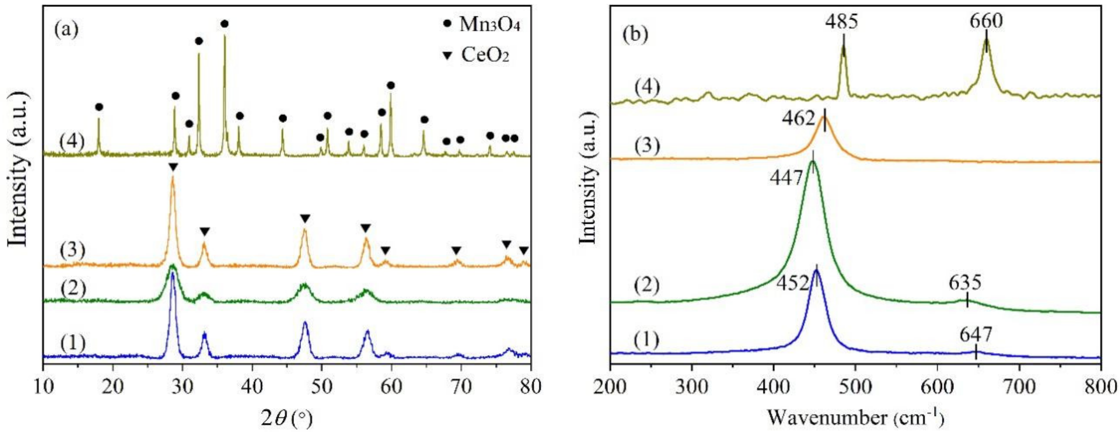

Figure 2. (**a**) XRD patterns and (**b**) Raman spectra of (1) MnCe-L, (2) MnCe-H, (3) CeO_2 and (4) Mn_3O_4.

Table 1. Structural properties of the catalysts.

Catalyst	Lattice Parameter (nm)	Crystallite Size (nm)	S_{BET} ($m^2 \cdot g^{-1}$)
MnCe-L	$a = b = c = 0.5387$	6.9	96
MnCe-H	$a = b = c = 0.5382$	4.2	126
CeO_2	$a = b = c = 0.5394$	6.7	98
Mn_3O_4	$a = b = 0.5754$; $c = 0.9432$	36.3	23

Raman spectroscopy was applied to obtain additional information of both M-O band and lattice defects, and the results are shown in Figure 2b. The bands at 485 and 660 cm^{-1} can be attributed to the stretching mode of the Mn-O lattice of Mn_3O_4 [22]. CeO_2 exhibits a distinct at 462 cm^{-1} assigned to a vibration mode of F_{2g} symmetry. This band shifts towards lower wavenumbers to different degrees for the mixed oxides. Such red shifts are related to the creation of more oxygen vacancies, or the expansion of the crystal cell [23]. According to the XRD results, the latter possibility can be excluded. Thus, the red shifts correspond to nonstoichiometry of $CeO_{2-\delta}$. The greater shift degree of MnCe-H is attributed to a more significant change of CeO_2 environment interacted by the substituted high-valent Mn^{4+} and Mn^{3+} cations. The ceria band is symmetrical and remains undisturbed by the manganese oxide feature at 485 cm^{-1}. Additionally, the spectrum of the Mn_3O_4 + CeO_2 mixture (not shown) exhibits not only the characteristics of CeO_2 at 456 cm^{-1} but also that of Mn_3O_4 at 653 cm^{-1}. Herein, the bands at 635 and 647 cm^{-1} are associated with the oxygen vacancies induced by the generation of Ce^{3+} [19,24], which show a similar shift trend with the main band. These oxygen vacancies are conducive to the diffusion of lattice oxygen, further promoting the oxidation reaction.

Figure 3 shows the deconvoluted XPS spectra of the two $Mn_{0.15}Ce_{0.85}O_{2-\delta}$ mixed oxides. As shown in Figure 3a, the Mn 2$p_{3/2}$ spectra reveal three main peaks at 640.5, 641.7 and 642.6 eV attributed to the presence of Mn^{2+}, Mn^{3+} and Mn^{4+}, respectively [25,26]. The peak at 646.0 eV is the shakeup satellite of divalent Mn bound to O as the charge-transfer compound [24]. The relative percentage of Mn^{2+} was calculated by the peak area ratio of $Mn^{2+}/(Mn^{2+} + Mn^{3+} + Mn^{4+})$. Obviously, the $Mn(NO_3)_2$-derived MnCe-L processes more Mn^{2+} (40.6%) than the $KMnO_4$-dervied one (27.6%). That is, the choice of the Mn precursor affects the oxidation state of manganese ions in the obtained products.

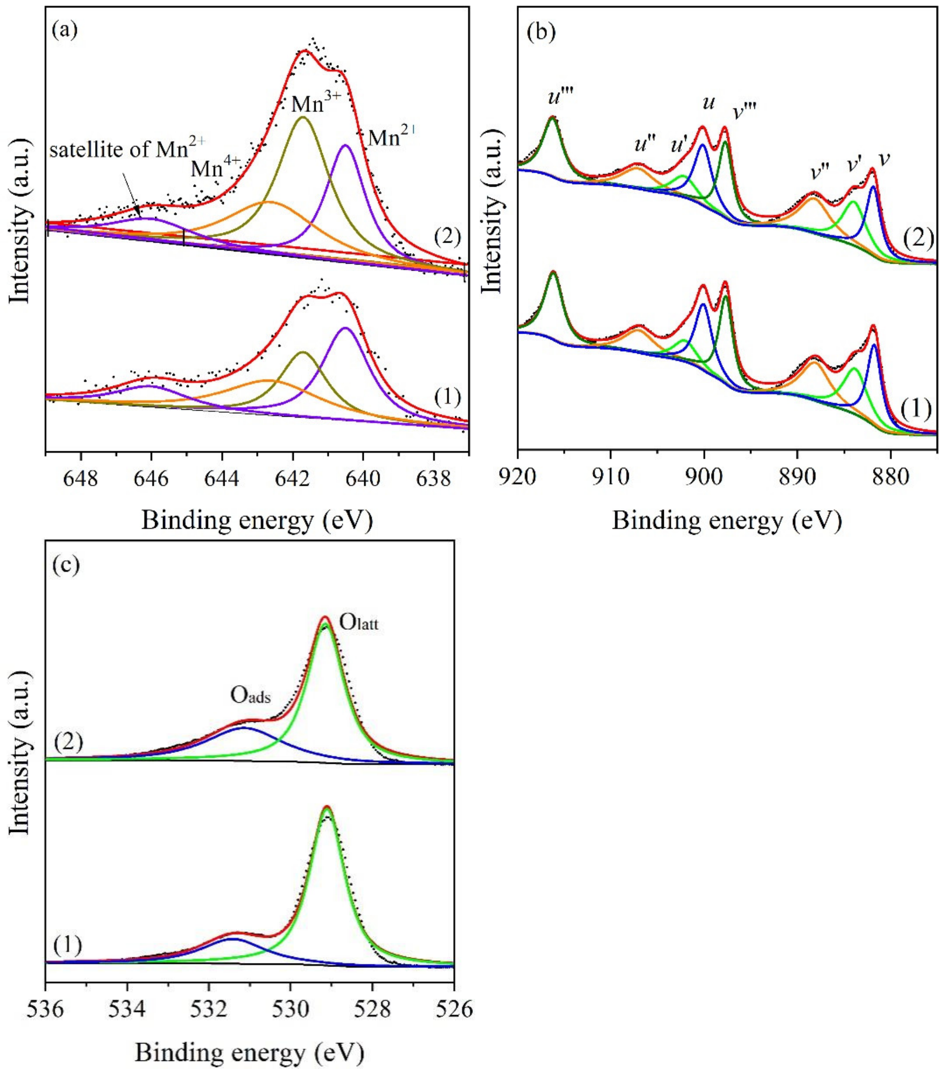

Figure 3. XPS spectra of (**a**) Mn 2$p_{3/2}$, (**b**) Ce 3d and (**c**) O 1s on (1) MnCe-L and (2) MnCe-H.

Figure 3b shows the XPS spectra of Ce 3d fitted with eight peaks, including those of Ce^{4+} 3$d_{3/2}$ (u, u'' and u'''), Ce^{4+} 3$d_{5/2}$ (v, v'' and v'''), Ce^{3+} 3$d_{3/2}$ (u'), and Ce^{3+} 3$d_{5/2}$ (v'). The relative percentage of Ce^{3+} was calculated by the peak area ratio of $v'/(v + v' + v'' + v''')$. The obtained surface Ce^{3+}/Ce ratio on MnCe-H (25.7%) is somewhat higher than that on MnCe-L (23.8%). The changes are not so significant for the multiple splitting of the Ce 3d signals, which may be related to the dominant content of Ce in the mixed oxides. According to Machida's work [11], it is plausible for Mn^{3+} to substitute Ce^{4+} in the fluorite structure when considering their structural similarity, although their ionic radius are quite different. In the present work, the introduction of more Mn^{3+} instead of Mn^{2+} in MnCe-H produces more Ce^{3+} due to the electronic equilibrium and structural stability since Ce^{3+} has a lower oxidation state and a larger ionic radius than Ce^{4+}.

The formation of Ce^{3+} can also produce more oxygen vacancy and adsorbed oxygen species, which is confirmed by the XPS spectra of O 1*s* in Figure 3c. The peaks at 529.4 and 531.9 eV are characteristic of lattice oxygen (O_{latt}) and surface adsorbed oxygen (O_{ads}), respectively [27]. The relative percentage of O_{ads} was calculated by the peak area ratio of $O_{ads}/(O_{latt} + O_{ads})$. More adsorbed oxygen (33.1%) is detected on the surface of MnCe-H than on MnCe-L (22.3%), accompanied with a high ratio of Ce^{3+}.

3.3. Redox Properties

The reducibility of metal ions was investigated by H_2-TPR. Figure 4a shows the reduction profiles of Mn_3O_4, CeO_2 and the co-precipitated mixed oxides. CeO_2 has two typical peaks at 475 and 692 °C assigned to the reduction of surface/subsurface Ce^{4+} and bulk Ce^{4+}, respectively. Mn_3O_4 shows a broad peak at 394 °C due to reduction of Mn^{3+} to Mn^{2+}. The calculated H_2 consumption (1720 μmol·g^{-1}) is much smaller than the theoretical value (4370 μmol·g^{-1}) for the reduction of Mn_3O_4 to MnO, which is mainly caused by the difficult reduction of large manganese oxides [28]. A shoulder at 168 °C belongs to the reduction of surface MnO_2 clusters to Mn_3O_4 [29], although they cannot be detected by XRD.

Compared with Mn_3O_4, MnCe-L and especially MnCe-H show a similar but much stronger peak at 177–199 °C, which implies the generation of more Mn^{4+} in the mixed oxides. The calculated H_2 consumption for the first deconvoluted peak in MnCe-H (624 μmol·g^{-1}) is larger than that in MnCe-L (568 μmol·g^{-1}). Meanwhile, the second peak shifts towards lower temperatures (276–321 °C). The calculated H_2 consumption for this peak is 804 and 989 μmol·g^{-1} for MnCe-H and MnCe-L, respectively. These data are larger than the theoretical value (321 μmol·g^{-1}) by assuming that all manganese ions in the mixed oxides exist in the form of Mn_3O_4 and MnO is the final product. Herein, it is ascribed not only to the reduction of Mn_3O_4 to MnO but also to that of CeO_2 to Ce_2O_3 promoted by Mn^{x+} in the solid solutions or at the interface. Similarly, the promoted reduction of Ce^{4+} may also contribute to the first peak. Those small peaks at 361–458 °C are suggested to be associated with the reduction of less affected Mn_3O_4 and CeO_2. The high-temperature peaks at 713–729 °C are assigned to the reduction of bulk oxygen from ceria unpromoted with Mn.

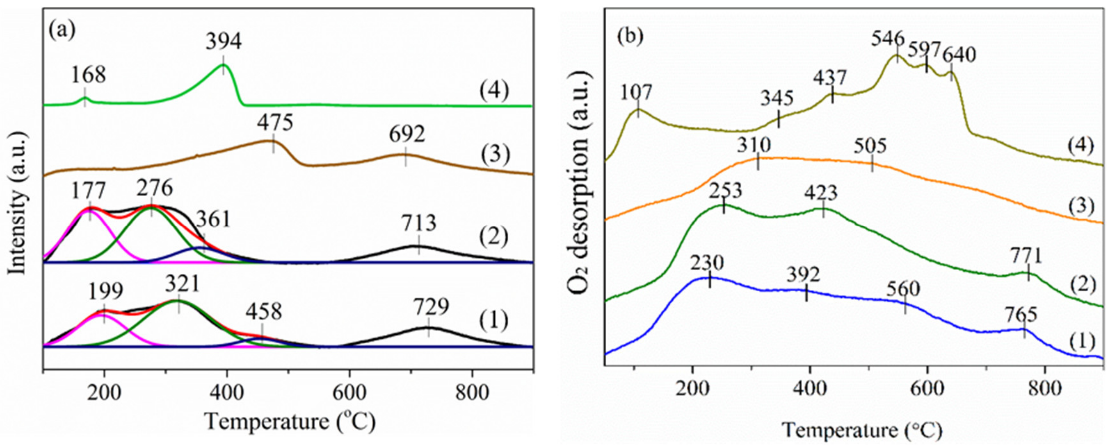

Figure 4. (**a**) H_2-TPR and (**b**) O_2-TPD profiles of (1) MnCe-L, (2) MnCe-H, (3) CeO_2 and (4) Mn_3O_4.

The O_2-TPD technique was used to determine the reactivity of oxygen species of metal oxides. As shown in Figure 4b, the peak at 107 °C is related to desorption of superoxide ion O_2^- on the Mn_3O_4 surface [30]. The peaks at 345 and 437 °C are assigned to the desorption of chemisorbed oxygen species [31]. The peaks range from 450 to 650 °C are associated with the surface lattice oxygen species [25]. Overlapped broad peaks, which are attributed to the reduction of superoxide ions O_2^- and peroxide ions O_2^{2-}/O^- on the surface, are observed for CeO_2 [32]. The desorption curves of the mixed oxides are more complicated. The distinct peaks at 230–253 °C and 392–423 °C are attributed to the desorption of surface-active oxygen species bound to oxygen vacancies (i.e., O^{2-} and O^-) and the coordinately unsaturated surface lattice oxygen, respectively [33]. It can be seen by integrating the peak area that more surface-active oxygen species are produced on MnCe-H than on MnCe-L. It implies that the strong metal-metal interaction in the MnCe-H results in more lattice defects (such as oxygen vacancies) and facilitates the creation of active O_2^{2-}/O^-. The peak at around 560 °C is related to the coordinately saturated surface lattice oxygen species. The desorption peaks at 765–771 °C are attributed to lattice oxygen ion O^{2-} from CeO_2 promoted by Mn^{x+} [34]. It suggests that the incorporation of Mn into ceria enhances the mobility of lattice oxygen. These results are consistent with the H_2-TPR results.

4. Conclusions

$Mn(NO_3)_2$ and $KMnO_4$ were applied as the manganese precursors to synthesize $Mn_{0.15}Ce_{0.85}O_{2-\delta}$ mixed oxides by coprecipitation, respectively. Manganese existed mainly in a pseudo-solid solution with a fluorite-type structure of CeO_2. The application of $KmnO_4$ leads to a higher proportion of Mn^{4+} and Mn^{3+} in the mixed oxide than that in the $Mn(NO_3)_2$-dervied one. The incorporation of Mn^{4+} and Mn^{3+} into the ceria lattice results in the formation of more Ce^{3+} due to the electronic equilibrium and structural stability. Herein, more oxygen vacancies and active oxygen species are created on the former catalyst, resulting in a maximum NO conversion of 64% achieved at 331 °C for NO oxidation.

Author Contributions: Experimental preparation and operation, analysed data, writing—original draft, and employment of software, Y.G. and B.J.; conceptualization, writing—review and editing, and supervision, X.W.; analysed data and funding acquisition, Z.L., R.R., and D.W. All authors have read and agreed to the published version of the manuscript.

Funding: This research was funded by the National Engineering Laboratory for Mobile Source Emission Control Technology (No. NELMS2020A08) and the Key Laboratory of Advanced Materials of Ministry of Education of China (Grant No. ADV22-18).

Conflicts of Interest: The authors declare no conflict of interest.

References

1. Zhang, H.; Zhou, C.; Galvez, M.; Costa, P.; Chen, Y.; MnOx-CeO2 mixed oxides as the catalyst for NO-assisted soot oxidation: The key role of NO adsorption/desorption on catalytic activity. *Appl. Surf. Sci.* **2018**, *462*, 678–684.
2. Zhao, S.; Peng, J.; Ge, R.; Wu, S.; Zeng, K.; Huang, H.; Yang, K.; Sun, Z. Research progress on selective catalytic reduction (SCR) catalysts for NOx removal from coal-fired flue gas. *Fuel Process. Technol.* **2022**, *236*, 107432.
3. Irfan, M.F.; Goo, J.H.; Kim, S.D. Co3O4 based catalysts for NO oxidation and NOx reduction in fast SCR process. *Appl. Catal. B Environ.* **2008**, *78*, 267–274. https://doi.org/10.1016/j.apcatb.2007.09.029.
4. Song, J.H.; Park, D.C.; You, Y.-W.; Kim, Y.J.; Lee, J.H.; Heo, I.; Kim, D.H. Promotive effects of Ba addition on lean NOx reduction by CO over IrRu/Al2O3 catalyst. *Chem. Eng. J.* **2023**, *452*, 139331. https://doi.org/10.1016/j.cej.2022.139331.
5. Wasalathanthri, N.D.; SantaMaria, T.M.; Kriz, D.A.; Dissanayake, S.L.; Kuo, C.-H.; Biswas, S.; Suib, S.L. Mesoporous manganese oxides for NO2 assisted catalytic soot oxidation. *Appl. Catal. B Environ.* **2017**, *201*, 543–551. https://doi.org/10.1016/j.apcatb.2016.08.052.
6. Wang, P.; Li, Z.; Ao, C.; Zhang, L.; Lei, L. Interactive effects of NOx synergistic and hydrothermal aging on soot catalytic combustion in Ce-based catalysts. *Combust. Flame* **2022**, *245*, 112289. https://doi.org/10.1016/j.combustflame.2022.112289.
7. Tang, A.; Hu, L.; Yang, X.; Jia, Y.; Zhang, Y. Promoting effect of the addition of Ce and Fe on manganese oxide catalyst for 1,2-dichlorobenzene catalytic combustion. *Catal. Commun.* **2016**, *82*, 41–45. https://doi.org/10.1016/j.catcom.2016.04.015.
8. Du, J.; Qu, Z.; Dong, C.; Song, L.; Qin, Y.; Huang, N. Low-temperature abatement of toluene over Mn-Ce oxides catalysts synthesized by a modified hydrothermal approach. *Appl. Surf. Sci.* **2018**, *433*, 1025–1035. https://doi.org/10.1016/j.apsusc.2017.10.116.
9. Jin, B.; Wu, X.; Weng, D.; Liu, S.; Yu, T.; Zhao, Z.; Wei, Y. Roles of cobalt and cerium species in three-dimensionally ordered macroporous CoxCe1-xOδ catalysts for the catalytic oxidation of diesel soot. *J. Colloid Interface Sci.* **2018**, *532*, 579–587.
10. Wang, Q.; Li, L.; Huang, T.; Ding, J.; Lu, Y.; Liang, B.; Liu, H.; Li, G. Sequencing the CuOx active species for CO preferential oxidation at low-temperature over CeO2-CuO composite catalysts. *Chem. Eng. J.* **2023**, *452*, 139467. https://doi.org/10.1016/j.cej.2022.139467.

11. Machida, M.; Uto, M.; Kurogi, D.; Kijima, T. Solid-gas interaction of nitrogen oxide adsorbed on MnOx-CeO2: A DRIFTS study. *J. Mater. Chem.* **2001**, *11*, 900–904.
12. Machida, M.; Uto, M.; Kurogi, D.; Kijima, T. MnOx-CeO2 binary oxides for catalytic NOx sorption at low temperatures. sorptive removal of NOx. *Chem. Mater.* **2000**, *12*, 3158–3164.
13. Li, H.; Tang, X.; Yi, H.; Yu, L. Low-temperature catalytic oxidation of NO over Mn-Ce-Ox catalyst. *J. Rare Earths* **2010**, *28*, 64–68. https://doi.org/10.1016/s1002-0721(09)60052-1.
14. Wu, X.; Yu, H.; Weng, D.; Liu, S.; Fan, J. Synergistic effect between MnO and CeO2 in the physical mixture: Electronic interaction and NO oxidation activity. *J. Rare Earths* **2013**, *31*, 1141–1147. https://doi.org/10.1016/s1002-0721(12)60418-9.
15. Xu, Q.; Fang, Z.; Chen, Y.; Guo, Y.; Wang, L.; Wang, Y.; Zhang, J.; Zhan, Wang. Titania-Samarium-Manganese Composite Oxide for the Low-Temperature Selective Catalytic Reduction of NO with NH3. *Environ. Sci. Technol.* **2020**, *54*, 2530–2538.
16. Fang, X.; Liu, Y.; Cheng, Y.; Cen, W. Mechanism of Ce-Modified Birnessite-MnO2 in Promoting SO2 Poisoning Resistance for Low-Temperature NH3-SCR. *ACS Catal.* **2021**, *11*, 4125–4135.
17. Zhao, B.; Ran, R.; Wu, X.; Weng, D. Phase structures, morphologies, and NO catalytic oxidation activities of single-phase MnO2 catalysts. *Appl. Catal. A Gen.* **2016**, *514*, 24–34.
18. Wu, X.; Liu, S.; Weng, D.; Lin, F. Textural-structural properties and soot oxidation activity of MnOx-CeO2 mixed oxides. *Catal. Commun.* **2011**, *12*, 345–348.
19. Liao, Y.; Fu, M.; Chen, L.; Wu, J.; Huang, B.; Ye, D. Catalytic oxidation of toluene over nanorod-structured Mn–Ce mixed oxides. *Catal. Today* **2013**, *216*, 220–228. https://doi.org/10.1016/j.cattod.2013.06.017.
20. Xiao, Y.; Wu, X.; Liu, S.; Wan, J.; Li, M.; Weng, D.; Tong. C. Modification of PdO/CeO2-ZrO2 catalyst by MnOx for water-gas shift reaction: Redox property and valence state of Pd. *J. Mater. Sci.* **2016**, *51*, 5377–5387.
21. Zhu, Y.; Wang, Q.; Lan, L.; Chen, S.; Zhang, J. Effect of surface manganese oxide species on soot catalytic combustion of Ce–Mn–O catalyst. *J. Rare Earths* **2022**, *40*, 1238–1246. https://doi.org/10.1016/j.jre.2021.08.017.
22. Silva, G.C.; Almeida, F.S.; Dantas, M.S.S.; Ferreira, A.M.; Ciminelli, V.S. Raman and IR spectroscopic investigation of As adsorbed on Mn3O4 magnetic composites. *Spectrochim. Acta Part A Mol. Biomol. Spectrosc.* **2013**, *100*, 161–165. https://doi.org/10.1016/j.saa.2012.04.061.
23. McBride, J.R.; Hass, K.C.; Poindexter, B.D.; Weber, W.H. Raman and x-ray studies of Ce1−xRExO2−y, where RE=La, Pr, Nd, Eu, Gd, and Tb. *J. Appl. Phys.* **1994**, *76*, 2435.
24. You, X.; Sheng, Z.; Yu, D.; Yang, L.; Xiao, X.; Wang, S. Influence of Mn/Ce ratio on the physicochemical properties and catalytic performance of graphene supported MnOx-CeO2 oxides for NH3-SCR at low temperature. *Appl. Surf. Sci.* **2017**, *423*, 845–854.
25. Mo, S.; Zhang, Q.; Li, J.; Sun, Y.; Ren, Q.; Zou, S.; Zhang, Q.; Lu, J.; Fu, M.; Mo, D.; et al. Highly efficient mesoporous MnO2 catalysts for the total toluene oxidation: Oxygen-Vacancy defect engineering and involved intermediates using in situ DRIFTS. *Appl. Catal. B Environ.* **2020**, *264*, 118464. https://doi.org/10.1016/j.apcatb.2019.118464.
26. Iwanowski, R.; Heinonen, M.; Janik, E. X-ray photoelectron spectra of zinc-blende MnTe. *Chem. Phys. Lett.* **2004**, *387*, 110–115. https://doi.org/10.1016/j.cplett.2004.01.109.s
27. Zhang, L.; Shu, H.; Jia, Y.; Lei, Z.; Bai, F.; Kuang, W.; Qi, L.; Shang, J.; Chao, W. Study on denitration and sulfur removal performance of Mn-Ce supported fly ash catalyst. *Chemosphere* **2021**, *270*, 128646.
28. Ji, Y.; Duan, A.; Jiang, G.; Liu, J. Comparative study on the formation and reduction of bulk and Al2O3-supported cobalt oxides by H2-TPR technique. *J. Phys. Chem. C* **2009**, *113*, 7186–7199.
29. Lin, R.; Liu, W.-P.; Zhong, Y.-J.; Luo, M.-F. Co Oxidation Activity And Tpr Characterization Of Ag-Mn Complex Oxide Catalysts. *React. Kinet. Catal. Lett.* **2001**, *72*, 289–295. https://doi.org/10.1023/a:1010594929479.
30. Liang, H.; Hong, Y.; Zhu, C.; Li, S.; Chen, Y.; Liu, Z.; Ye, D. Influence of partial Mn-substitution on surface oxygen species of LaCoO3 catalysts. *Catal. Today* **2013**, *201*, 98–102. https://doi.org/10.1016/j.cattod.2012.04.036.
31. Jampaiah, D.; Velisoju, V.; Devaiah, D.; Singh, M.; Mayes, E.; Coyle, V.; Reddy, B.; Bansal, V.; Bhargava, S. Flower-like Mn3O4/CeO2 microspheres as an efficient catalyst for diesel soot and CO oxidation: Synergistic effects for enhanced catalytic performance. *Appl. Surf. Sci.* **2019**, *473*, 209–221.
32. Lin, X.; Li, S.; He, H.; Wu, Z.; Wu, J.; Chen, L.; Ye, D.; Fu, M. Evolution of oxygen vacancies in MnOx-CeO2 mixed oxides for soot oxidation. *Appl. Catal. B Environ.* **2018**, *223*, 91–102.
33. Sun, H.; Yu, X.; Yang, X.; Ma, X.; Lin, M.; Shao, C.; Zhao, Y.; Wang, F.; Ge, M. Au/Rod-like MnO2 catalyst via thermal decomposition of manganite precursor for the catalytic oxidation of toluene. *Catal. Today* **2019**, *332*, 153–159. https://doi.org/10.1016/j.cattod.2018.07.017.
34. Liang, Q.; Wu, X.; Weng, D.; Xu, H. Oxygen activation on Cu/Mn–Ce mixed oxides and the role in diesel soot oxidation. *Catal. Today* **2008**, *139*, 113–118. https://doi.org/10.1016/j.cattod.2008.08.013.